

## Simulations of the Atmospheric General Circulation Using a Cloud-Resolving Model as a Superparameterization of Physical Processes

MARAT KHAIROUTDINOV, DAVID RANDALL, AND CHARLOTTE DEMOTT

*Department of Atmospheric Science, Colorado State University, Fort Collins, Colorado*

(Manuscript received 12 June 2003, in final form 25 May 2004)

### ABSTRACT

Traditionally, the effects of clouds in GCMs have been represented by semiempirical parameterizations. Recently, a cloud-resolving model (CRM) was embedded into each grid column of a realistic GCM, the NCAR Community Atmosphere Model (CAM), to serve as a superparameterization (SP) of clouds. Results of the standard CAM and the SP-CAM are contrasted, both using T42 resolution ( $2.8^\circ \times 2.8^\circ$  grid), 26 vertical levels, and up to a 500-day-long simulation. The SP was based on a two-dimensional (2D) CRM with 64 grid columns and 24 levels collocated with the 24 lowest levels of CAM. In terms of the mean state, the SP-CAM produces quite reasonable geographical distributions of precipitation, precipitable water, top-of-the-atmosphere radiative fluxes, cloud radiative forcing, and high-cloud fraction for both December–January–February and June–July–August. The most notable and persistent precipitation bias in the western Pacific, during the Northern Hemisphere summer of all the SP-CAM runs with 2D SP, seems to go away through the use of a small-domain three-dimensional (3D) SP with the same number of grid columns as the 2D SP, but arranged in an  $8 \times 8$  square with identical horizontal resolution of 4 km. Two runs with the 3D SP have been carried out, with and without explicit large-scale momentum transport by convection. Interestingly, the double ITCZ feature seems to go away in the run that includes momentum transport.

The SP improves the diurnal variability of nondrizzle precipitation frequency over the standard model by precipitating most frequently during late afternoon hours over the land, as observed, while the standard model maximizes its precipitation frequency around local solar noon. Over the ocean, both models precipitate most frequently in the early morning hours as observed. The SP model also reproduces the observed global distribution of the percentage of days with nondrizzle precipitation rather well. In contrast, the standard model tends to precipitate more frequently, on average by about 20%–30%. The SP model seems to improve the convective intraseasonal variability over the standard model. Preliminary results suggest that the SP produces more realistic variability of such fields as 200-mb wind and OLR, relative to the control, including the often poorly simulated Madden–Julian oscillation (MJO).

### 1. Introduction

Among the many atmospheric processes that play a role in climate, cloud processes are among the most important and also among the most difficult to understand and predict. Cloud processes affect the climate system by regulating the flow of radiation at the top of the atmosphere, by controlling precipitation, and through numerous other mechanisms. Complicated dynamical processes associated with the motion of the air on the scale of clouds are further complicated by cloud microphysics involving cloud drops, ice crystals, and aerosols as well as by radiative transfer that depends strongly on local emission, absorption, and scattering by clouds. These physical processes interact with each other on cloud scales that can be as small as a few

hundred meters, and time scales of just a few minutes. Collectively the processes interact with the larger-scale atmosphere circulations. Because global climate models (GCMs) have grid resolution on the order of a few hundred kilometers, these cloud-scale processes have not been explicitly represented.

Is it really possible to represent all of the complexity of clouds with quantitative accuracy? Since the onset of global climate modeling, various statistical theories of clouds, called parameterizations, have been developed to account for the effects of clouds in GCMs. These semiempirical parameterizations generally extrapolate the unresolved or subgrid-scale (SGS) information from the grid-resolved fields using some simple general rules. The modern parameterizations can be quite complex, and generally involve sets of free parameters that are deduced from observations or more detailed models, or simply tuned to make target simulations come into reasonable agreement with observations; however, no observations are available to tune the models when simulations of future climates are performed. Overall,

---

*Corresponding author address:* Marat Khairoutdinov, Department of Atmospheric Science, Colorado State University, Fort Collins, CO 80523.  
E-mail: marat@atmos.colostate.edu

the problem of cloud parameterization remains still largely unsolved and is in some sense “deadlocked,” as discussed by Randall et al. (2003a) and Arakawa (2004).

Unlike parameterizations, cloud-resolving models (CRMs) use the first-principle approach to modeling the dynamics of clouds with the exception of cloud microphysics, which is still highly parameterized. It has been demonstrated on the basis of several case studies that the CRMs’ results are better than the models that use parameterizations (e.g., Randall et al., 2003b). One may start dreaming about a global CRM as a climate model; however, it would take at least a million times more total computation time than current GCMs, just to start resolving the scales on the order of a few kilometers. At such resolution, only deep convective towers and storms would be resolved while the effects of other cloud types such as trade-wind cumulus or boundary layer stratocumulus would still be parameterized.

Recently, a new approach stimulated by the rapid progress of massively parallel computing has emerged. The approach, first suggested and implemented by Grabowski (2001), is a compromise between the “parameterize-everything” and “resolve-everything” pathways (Arakawa 2004) to global climate modeling. The approach roots itself from the single-column modeling (SCM; Betts and Miller 1986). In the SCM, a package of parameterizations from a GCM is forced by the prescribed tendencies representing large-scale advection usually estimated from observations. The results of parameterization response to such large-scale forcing are then compared to the observed response with the goal to reveal parameterization deficiencies and suggest improvements.

The CRMs have also been used in a similar manner (e.g., Xu and Randall 1996; Grabowski et al. 1998; Xu et al. 2002; Khairoutdinov and Randall 2003). Assuming complete scale separation between the large-scale and scales resolved by a CRM, the domain has usually been chosen to have no lateral boundaries, that is periodic, and the large-scale forcing is applied as horizontally uniform. Thus, a CRM is used much like a conventional parameterization, in that it receives the tendencies due to large-scale (or resolved-scale) processes as input, and returns the tendencies but due to “sub-large-scale” processes obtained by horizontal averaging of CRM fields as output. The important difference from the conventional parameterizations is that unlike the latter, the CRMs explicitly resolve most of the cloud dynamics and physical process interactions down to some scale defined by the CRM’s grid resolution and, thus, may be expected to react to the applied forcing in a more physically realistic manner.

The next logical step was to embed a CRM into each grid column of a GCM, and drive it with the large-scale forcing actually computed by the GCM itself. The idea is to generate a statistical sample of tendencies due to GCM’s subgrid-scale processes in response to applied

resolved-scale forcing. This statistical sample is then assumed to be the same over the whole GCM column, similar to the way that a population sample in an opinion poll is applied to the whole population.

Grabowski used the term “cloud-resolving cumulus parameterization” (CRCP) for such an embedded CRM. In his experiments, the CRCP was embedded into a simplified global model representing an aqua planet with globally uniform sea-surface temperatures (SSTs), no topography, etc. To limit the computational cost, a two-dimensional (2D) SP was applied with the results shown to be, to some extent, orientation-dependent. The periodicity of the domain in the SP approach precludes convective systems like squall lines from direct propagation to a neighbor GCM column.<sup>1</sup> Only implicit propagation can occur through the effects of convection on the large-scale circulation.

Khairoutdinov and Randall (2001; hereafter KR) took the SP a step further. They embedded a 2D version of their three-dimensional (3D) CRM into the National Center for Atmospheric Research (NCAR) Community Atmosphere Model (CAM), which is the atmosphere component of the Community Climate System Model (CCSM; Blackmon et al. 2001). The CAM has all the attributes of a true GCM: realistic SSTs, continents with topography, a sophisticated land surface model, convective and stratiform cloud parameterizations, a radiative transfer parameterization, etc. Khairoutdinov and Randall (2001) proposed the term “superparameterization” (hereafter SP) for such a CRM model when embedded in a GCM. As the initial test and, mainly, because of the limited computational resources available at the time of their study, KR performed a single 2-month (December–January) simulation using the combined model (referred further as SP-CAM) with T42 global-grid resolution and 26 levels. The simulated January-mean distribution of precipitation and precipitable water, as well as the earth’s radiation budget, looked very reasonable.

The results of KR encouraged us to perform an annual-cycle simulation with a relatively low-resolution T21 SP-CAM. The main goal was to see if the SP-CAM could simulate the Madden–Julian oscillation (MJO; Madden and Julian 1994). The results showed (Randall et al. 2003a) that the SP-CAM could indeed produce a vigorous MJO that has many features of the observed phenomenon, in contrast to the standard CAM, which produces virtually no MJO. Further encouraged by these results, we have recently performed a series of 500-day long T42 runs. This paper documents the details of the SP-CAM as well as the results from some of those runs.

An outline of the paper is as follows. Section 2 presents a brief description of the SP-CAM as well as the

---

<sup>1</sup> For the approaches that do not require periodical domains, see Randall et al. (2003a) and Arakawa (2004).

results of domain geometry and size sensitivity study. Section 3 shows some seasonally and zonally averaged results, characteristics of the simulated diurnal cycle, frequency of precipitation, short analysis of the tropical variability simulated by the models, and, finally, sensitivity of simulations to domain geometry. Section 4 offers a brief summary.

## 2. SP-CAM

### a. General description

As mentioned in the introduction, the CAM was used as the GCM component of the SP-CAM. We used the version 2.0.2, also known as CAM-2, as well as the development version of the so-called CAM-3 in most recent runs. The CAM was configured to run at T42 horizontal resolution ( $2.8^\circ \times 2.8^\circ$  grid) using 26 levels with the top at 3.5 mb. The CAM time step varied from case to case, from 1800 to 3600 s. The semi-Lagrangian dynamical core (Williamson and Olson 1994) was used in all runs mostly because of better scalability of the SP-CAM with that core on massively parallel computers.

The SP component of the SP-CAM is a modified version of a three-dimensional (3D) CRM described in detail by Khairoutdinov and Randall (2003). The SP solves the nonhydrostatic dynamical equations with the anelastic approximation. The prognostic thermodynamic variables include the liquid/ice-water moist static energy, the total nonprecipitating water, and the total precipitating water. The mixing ratio of cloud water, cloud ice, rain, snow and graupel are diagnosed from the prognostic variables using the partition between liquid and ice phases as the function of temperature. Bulk microphysics is applied to compute the hydrometeor conversion rates and terminal velocities. The model employs a finite-difference representation of the prognostic equations in flux form. The second-order central-difference method was used for the advection of momentum, while positively defined monotone algorithms were used for advection of all scalars. The model can be used in a 2D configuration.

A copy of the SP was embedded in each of the 8192 grid columns of CAM. Both 2D and 3D versions of the SP have been used in this study. The 2D version had 64 grid columns aligned in the west–east direction, while the 3D version had the same number of columns forming an  $8 \times 8$  horizontal grid. Both configurations used periodical lateral boundaries. The SP time step was 20 s. To limit computational cost, the horizontal grid spacing was 4 km, which is coarser than the spacing of 1–2 km typically used in CRM simulations of deep convection. The vertical grid had 24 levels collocated with the CAM’s grid levels.

### b. Coupling between the SP and CAM

Coupling between the SP and CAM is organized as follows. At the beginning of each simulation, the SP

fields in each CAM grid column are initialized by the CAM sounding. To initialize turbulence, small-amplitude noise is added to the SP temperature fields near the surface. No noise is added at later times. The SP is called on each CAM time step. The SP fields are initialized with the fields saved at the end of the previous call. The SP is thus continuously integrating its equations for the duration of the CAM time step, continuously forced by large-scale tendencies computed as

$$\left[ \frac{\partial \Phi}{\partial t} \right]_{\text{LS}} = \frac{\Phi_{\text{LS}} - \bar{\Phi}^n}{\Delta t_{\text{LS}}}, \quad (1)$$

where  $\Phi$  denotes any SP prognostic variable except precipitating water;  $\Phi_{\text{LS}}$  denotes the corresponding variable computed by the CAM as the result of all the large-scale processes after the SP call at the previous CAM time step; and  $\bar{\Phi}^n$  is the horizontally averaged SP variable at the end of the SP call at the previous CAM time step  $\Delta t_{\text{LS}}$ . In a nutshell, the large-scale forcing represents the relaxation of the SP horizontal averages to the provisional CAM fields. Clearly, the forcing term (1) by design does not allow systematic “drift” of the SP mean fields away from the corresponding CAM fields. The SP returns the large-scale tendencies due to the SP processes computed as

$$\left[ \frac{\partial \Phi}{\partial t} \right]_{\text{SP}} = \frac{\bar{\Phi}^{n+1} - \Phi_{\text{LS}}}{\Delta t_{\text{LS}}}, \quad (2)$$

where  $\bar{\Phi}^{n+1}$  is horizontal mean of the SP fields at the end of the SP call. It is obvious that the forcing in the form (1) ensures that in absence of cloud processes or convection resolved by the SP domain, the  $\bar{\Phi}^{n+1}$  will be identical to  $\Phi_{\text{LS}}$  at the end of the SP call, thus producing zero tendencies due to subgrid processes. Because of the unrealistic momentum transport associated with 2D cloud dynamics, no feedback to the large-scale wind due to the 2D SP processes was allowed. However, momentum feedback was allowed in the case of the 3D SP.

In the first version of the SP-CAM described by KR, the cloud–radiation interactions on cloud scale have not been included; that is, the radiative transfer was computed on the GCM grid using average profiles of cloud properties explicitly simulated by the SP. The standard CAM’s cloud-overlap assumptions were then employed. This was done for simplicity. We recognized, however, that there was little excuse for applying such rather arbitrary cloud-overlap assumptions having the explicitly simulated spatial distribution of clouds in the SP domain. In the current implementation of SP-CAM, the radiative transfer is done interactively within the SP domain, independently for each grid column, assuming 0-or-1 cloud fraction for each grid point. The radiative transfer is usually computed every 15 min, using the time-averaged SP fields. The overall increase of CPU time due to radiation computations in the SP domain is about 25%. We note that the very first numerical ex-

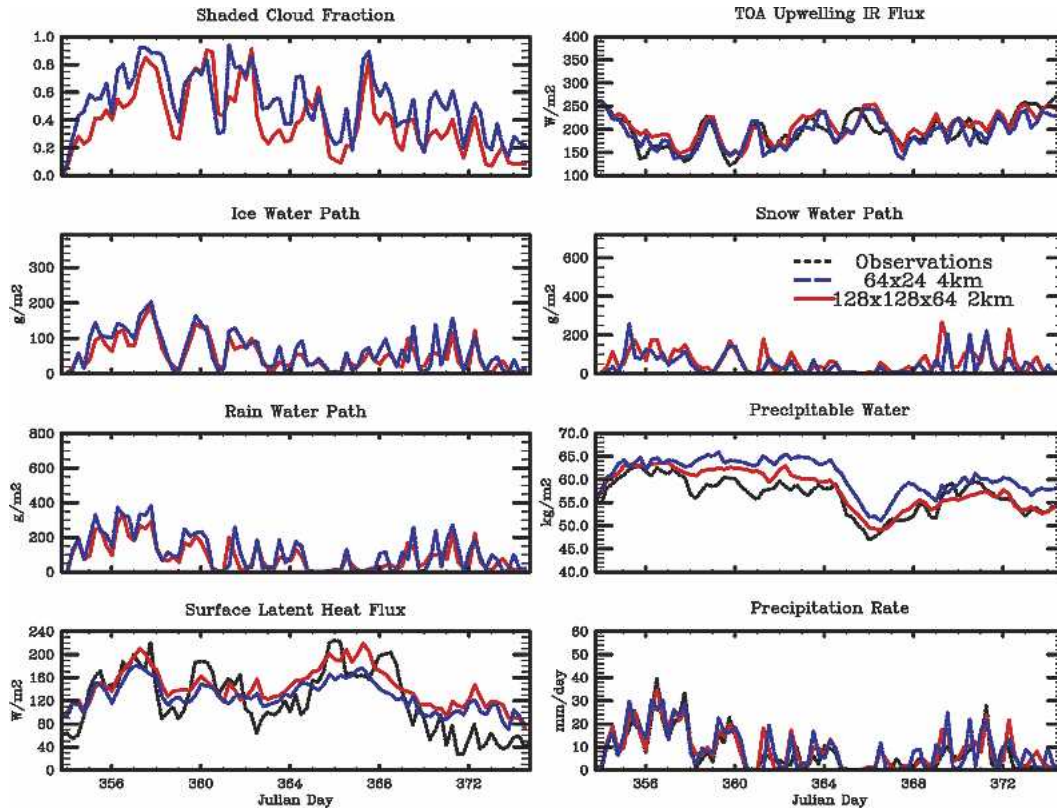


FIG. 1. Evolution of various 6-h running-mean fields for the TOGA COARE simulations with the 3D model with 2-km horizontal resolution and 64 vertical levels (solid red) and the 2D model used as a superparameterization with 4-km horizontal resolution and 24 vertical levels.

periments with the SP-CAM that included the explicit cloud-scale interactions between radiation and other cloud processes demonstrated that such cloud-scale interactions are quite important for determining the

large-scale distribution of cloudiness and cloud optical properties (Cole et al. 2005).

The surface models are currently coupled to the atmosphere model on the large-scale grid only—that is,

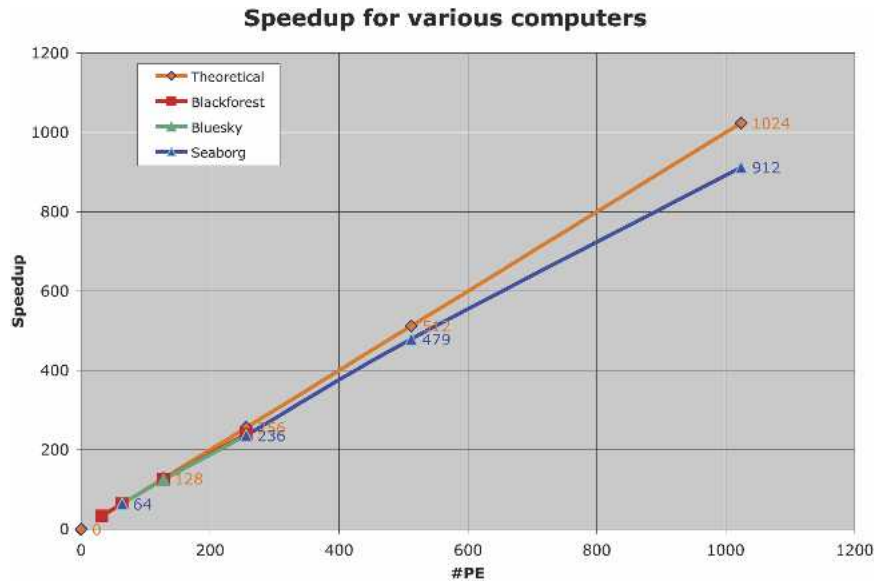


FIG. 2. Parallel performance of the SP-CAM on various IBM-SP supercomputers for various numbers of processors (PEs).

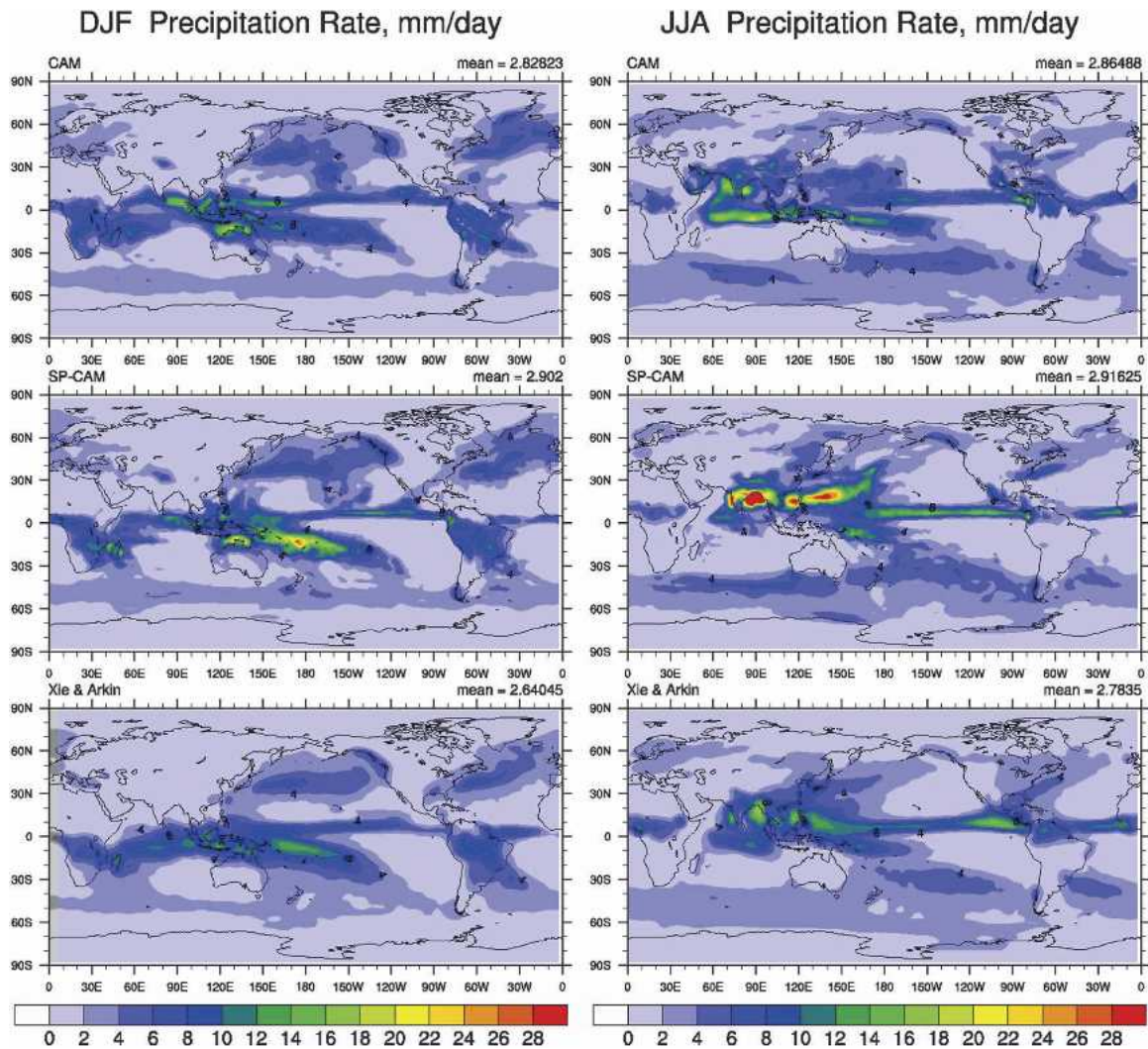


FIG. 3. Mean (left) DJF and (right) JJA total precipitation as simulated with the standard (upper) CAM, (middle) SP-CAM, and (lower) as observed.

the land surface fluxes are not computed at the scales of surface heterogeneity that are resolved by the SP, so no explicit effects of the local flux enhancement due to gust fronts, or due to local inhomogeneity of surface properties or soil moisture content, can be studied. These effects may be included in the future implementation of the SP-CAM. At present, only the local enhancement of the surface drag due to local perturbations of the near-surface wind is explicitly included.

### c. Grid size and resolution aspects

High computational cost of running the SP-CAM imposes rather severe constraint on size and resolution of the SP domain. In most of the SP-CAM runs carried out to date, the 2D SP domain was used. It had 64 grid columns with a rather coarse horizontal resolution of 4

km. The vertical resolution has in all cases been similar to the resolution of the host GCM to avoid the difficulties with interpolation from coarse to fine grids. Obviously, such grid is not generally sufficiently dense to resolve small boundary layer clouds such as trade cumuli. However, we assumed that it is sufficient to resolve such large cloud systems as deep 'hot towers', squall-lines with associated anvils, and large-scale clouds produced by the synoptic-scale processes such as cirrus.

The issues of resolution, domain size and geometry have always been a prime concern. Quite a few tests have been conducted using the single-column framework. The results of such experiments based on the Global Atmospheric Research Program (GARP) Atlantic Tropical Experiment (GATE) phase III observations have already been presented by KR. They basi-

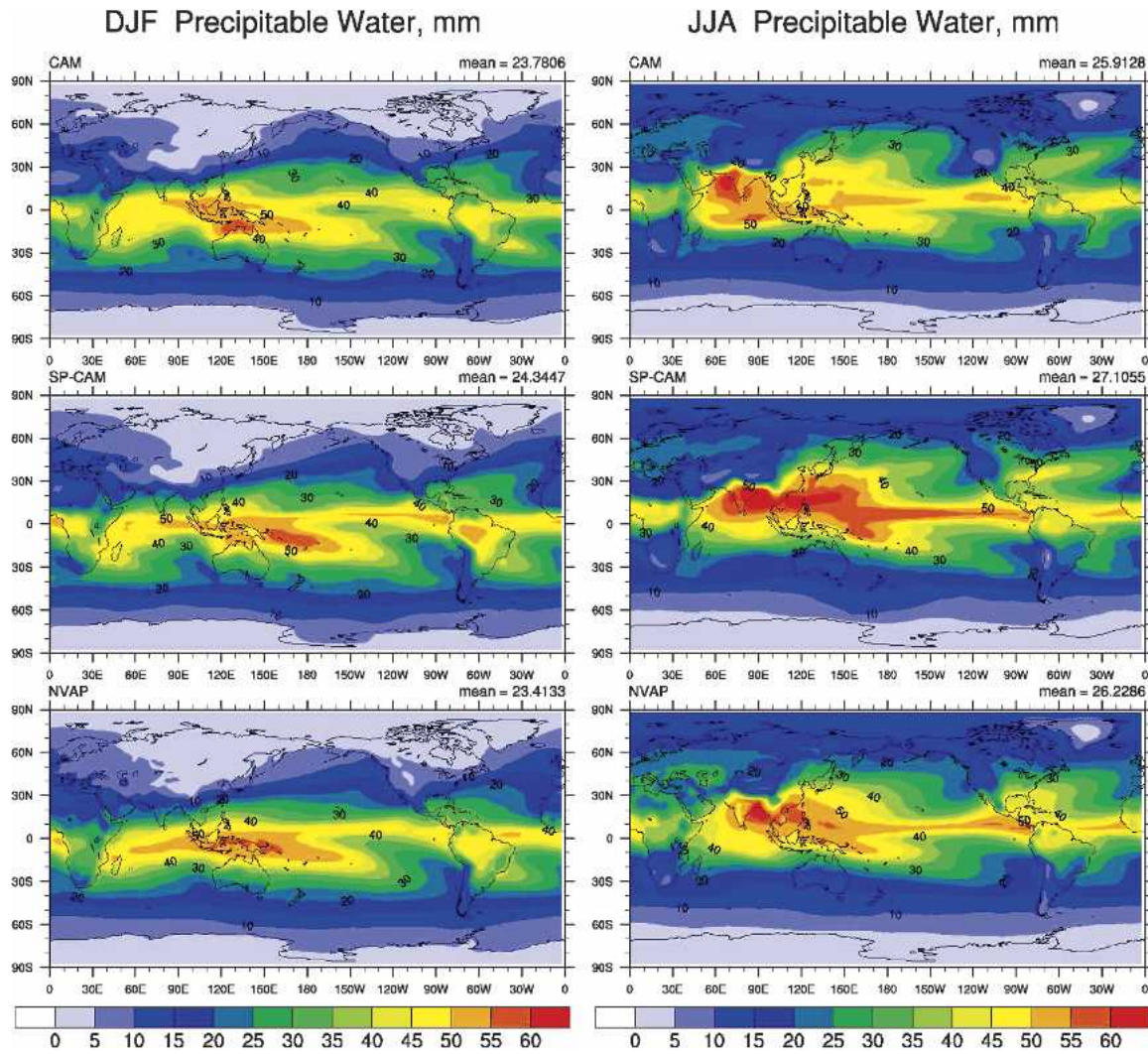


FIG. 4. As in Fig. 3, but for precipitable water.

cally concluded that the SP produces sufficiently accurate cloud statistics as compared to the 3D cloud-resolving model.

In more recent tests, we used the large-scale forcing derived from the Tropical Ocean and Global Atmosphere Coupled Ocean–Atmosphere Response Experiment (TOGA COARE) observations collected from 18 December 1992 to 8 January 1993. Unlike the GATE case presented by KR, where the radiative heating was a part of prescribed forcing, the radiative transfer in the TOGA case was computed. The low-resolution CRM used a 2D domain with  $64 \times 24$  grid points and horizontal resolution of 4 km and vertical resolution as in the version used for the CAM-SP. The benchmark simulation was produced by the 3D CRM that used  $128 \times 128 \times 64$  gridpoint domain with 2-km horizontal resolution and denser vertical grid. For example, 11 levels with the resolution stretching from 100 m near

the surface to 300 m at 2 km have been used below 2-km height. In contrast, the low-resolution CRM had only 5 levels below that altitude. In free troposphere, the 3D-CRM had uniform 500-m vertical resolution, while the SP had a roughly uniform resolution of about 1 km. Both models were forced by prescribed large-scale advection of static energy and water vapor. As mentioned above, the radiative heating rates as well as surface sensible and latent heat fluxes were interactive. The mean wind was nudged to the observed large-scale wind on a 2-h time scale.

Figure 1 compares the time series of several bulk parameters. One can see that there is hardly any significant discrepancy between the low-resolution CRM and 3D CRM simulations with the exception of some systematic positive bias in precipitable water for the SP case. The total shaded cloud fraction, outgoing long-wave radiation, as well as such cloud statistics as total

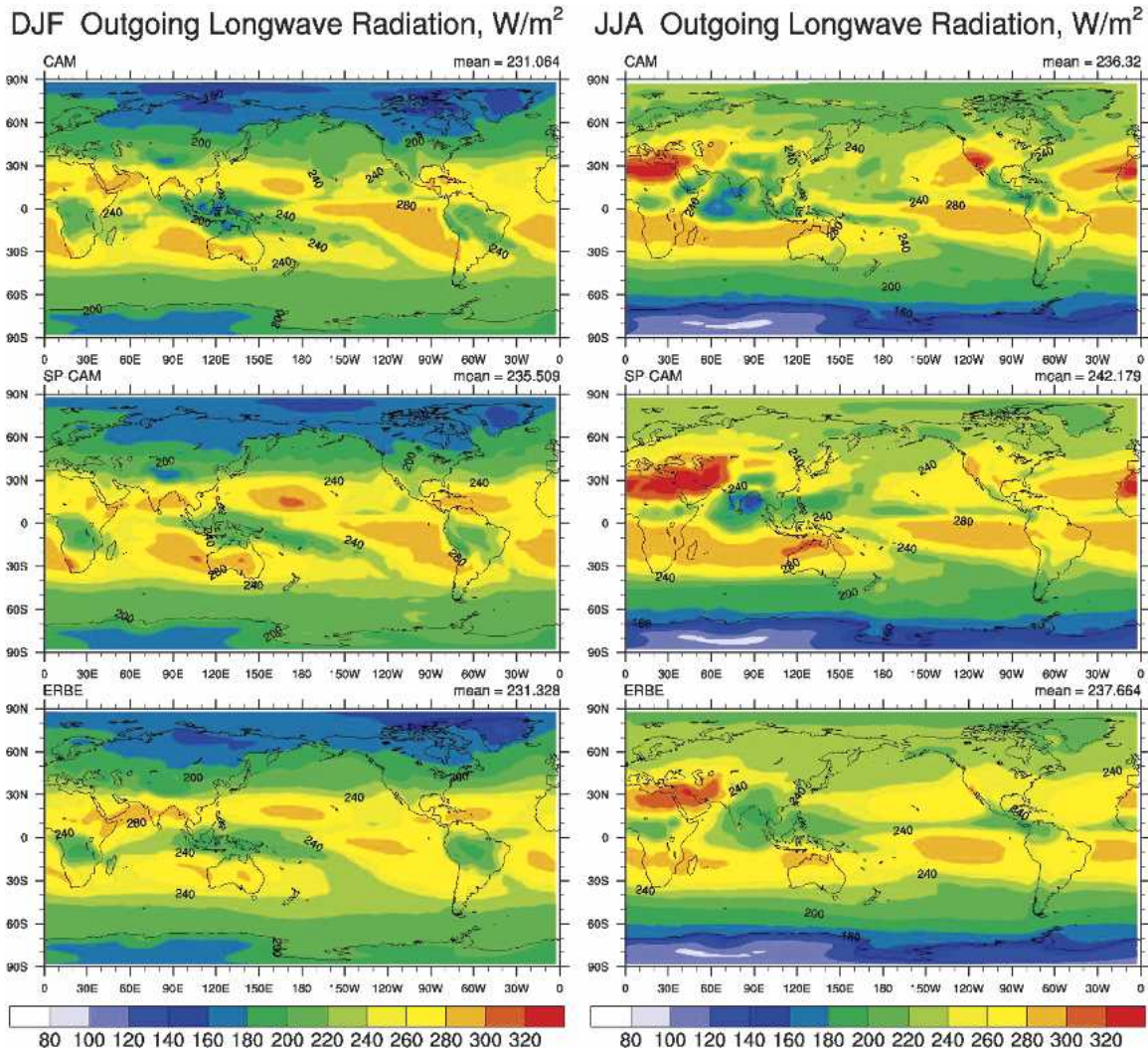


FIG. 5. As in Fig. 3, but for outgoing longwave radiation flux.

column cloud ice or total column snow/rain are quite similar. Despite poor resolution and 2D geometry, the low-resolution CRM seems to be capable of producing the result that closely resemble those obtained using a much denser 3D grid. This is quite remarkable, especially taking into account the fact that the low-resolution CRM uses about 2000 times less CPU time than its 3D counterpart.

We note, however, that such close agreement may be due to inherent limitations of the SCM framework, which does not allow feedbacks to the large-scale forcing. Prescribed forcing constrains the simulated thermodynamics, especially precipitation rates. For example, Khairoutdinov and Randall (2003) have demonstrated that the single-column modeling may represent a rather poor framework for revealing model deficiencies and sensitivities. The sensitivities may have been amplified had the feedbacks to the large-scale circula-

tion been somehow included. The SP-CAM allows such feedbacks.

#### d. Computational performance

The SP-CAM takes approximately 200 times more computation time than the conventional CAM; therefore, a good parallel performance of the model has been a crucial requirement. In early 2001, the prototype SP-CAM took more than 20 days of the wall-clock time to simulate one year at T42 resolution running on 64 processors of IBM-SP Blackforest supercomputer at NCAR. Two years later, due to software and hardware enhancements, we achieved almost linear scalability of the SP-CAM on 1024 processors of the IBM-SP Seaborg supercomputer at National Energy Research Scientific Computing Center (NERSC; U.S. Department of Energy) as shown by Fig. 2. Such parallel effi-

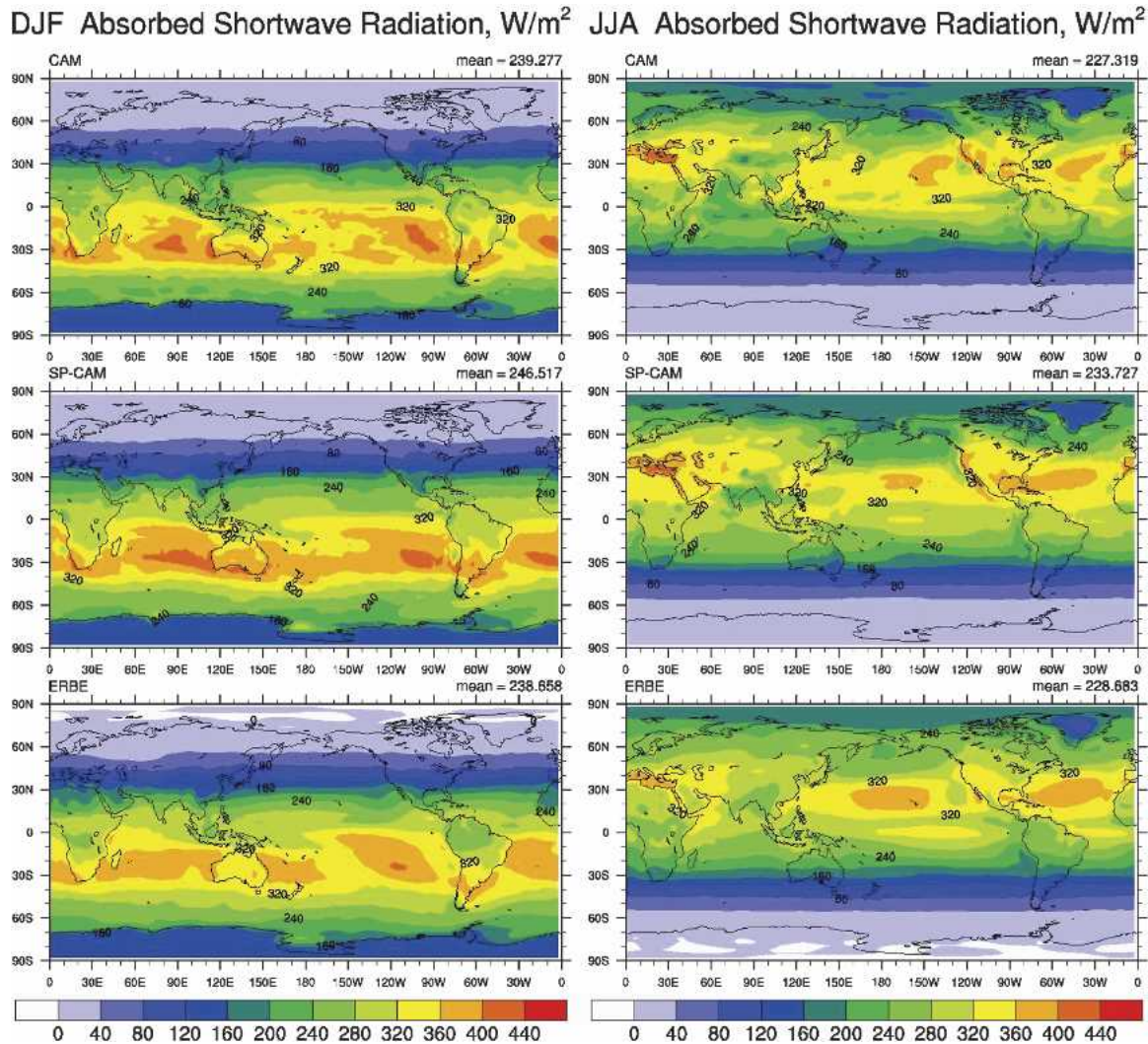


FIG. 6. As in Fig. 3, but for absorbed solar radiation flux.

ciency has allowed us to integrate 1 yr of general circulation at T42 resolution in less than two wall-clock days.

### 3. Results

Due to the large computational expense of running the SP-CAM and limited computational resources, only about a dozen integrations from 1 yr to 500 days in length have been completed since the first experiment described by KR. The results of the SP-CAM presented in this paper have been obtained using the latest version available at the time of writing this paper. The yearly mean top-of-atmosphere energy flux for that model has been less than  $2 \text{ W m}^{-2}$ .

The simulations were initialized on 1 September and integrated using the monthly mean climatological SSTs.

For reference, the results of the SP-CAM are supplemented by the results of the CAM with the standard set of parameterizations. Note that the results represent averages over just a few months, and therefore, are quite noisy when compared to observations that represent multiyear averages.

#### a. Mean state

Figure 3 shows the December–January–February (DJF) and June–July–August (JJA) mean global distribution of precipitation. The DJF pattern compared to the Xie and Arkin (1996) climatology is well reproduced by the SP-CAM showing well-simulated ITCZ and the South Pacific convergence zone (SPCZ), with the maximum precipitation over the SPCZ than over the ITCZ, as in observations. The Northern Hemisphere DJF extratropical storm tracks are also well

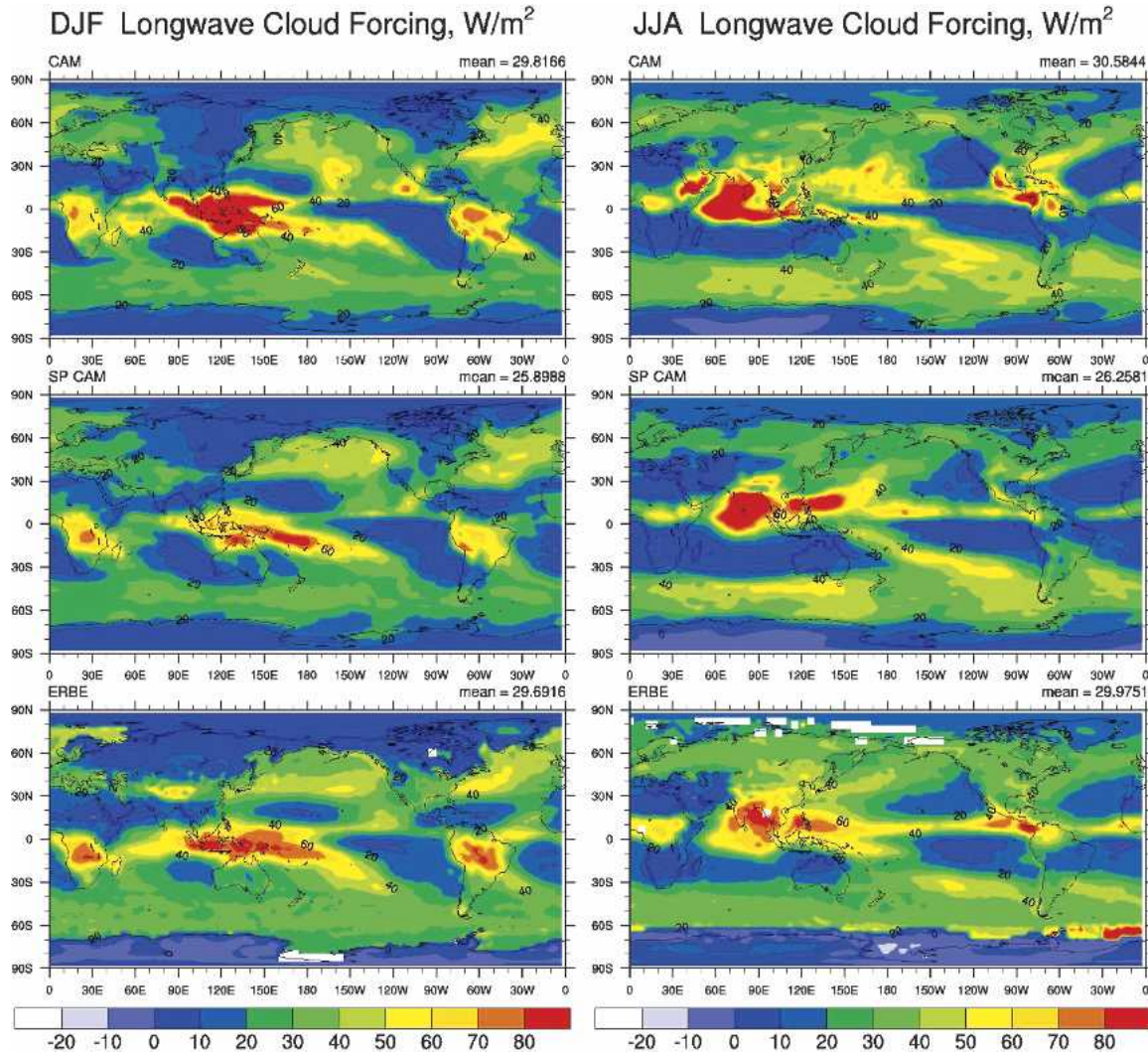


FIG. 7. As in Fig. 3, but for longwave cloud forcing.

simulated. The most serious biases in the SP-CAM simulation are revealed in the JJA season. One is the excessive precipitation in the Western Pacific associated with the Southeast Asian monsoon. This bias has been a robust feature of all the SP-CAM runs that use the 2D CRM as the SP. In the Indian Ocean region, there are intense precipitation maxima in the Bay of Bengal and Western India as observed, although their amplitude is overestimated. Unlike the control CAM, the SP-CAM avoids an unrealistic precipitation over the Arabian Peninsula. All simulations clearly exhibit a tendency to form a double ITCZ, especially during JJA.

The geographical distributions of precipitable water for DJF and JJA are shown in Fig. 4. For DJF, the SP-CAM represents a rather significant improvement over the control CAM in the overall geographical pattern. The JJA pattern is spoiled by the aforementioned Asian monsoon related precipitation anomaly. Overall,

the SP-CAM simulates a Tropics that is more humid than suggested by observations.

The distribution of the outgoing longwave radiation (OLR) is compared to Earth Radiation Budget Experiment (ERBE) in Fig. 5. In DJF, all three tropical regions of high deep convective activity, and therefore low OLR are well simulated. The subtropical OLR maxima are also rather well reproduced by the SP-CAM; however, the southeastern Pacific maximum is overestimated. In JJA, the overall pattern of OLR is rather well reproduced. The OLR over the Bay of Bengal is underestimated because of too vigorous convection, which is consistent with anomalously high precipitation. The top-of-atmosphere absorbed solar flux, shown in Fig. 6, is in fair agreement with ERBE, with most of the biases being in the subtropical regions where the SP-CAM underestimates the low-cloud amount due to coarse horizontal resolution of the SP grid.

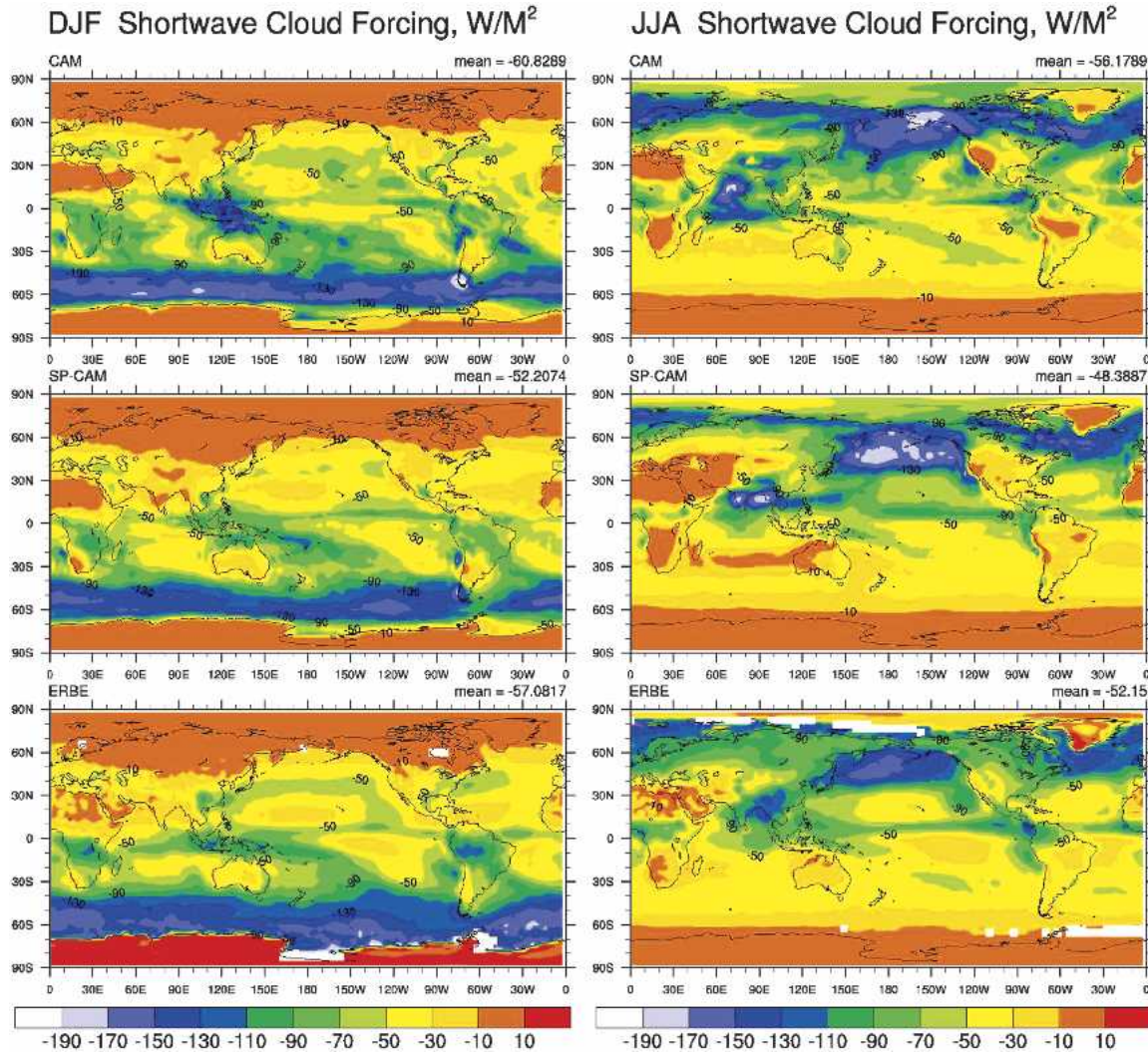


FIG. 8. As in Fig. 3, but for shortwave cloud forcing.

Radiative effects of clouds on global radiation fluxes at the top of atmosphere are best illustrated by the longwave (LWCF) and shortwave (SWCF) cloud forcing. The overall geographical pattern of the LWCF (Fig. 7) agrees well with ERBE. The most apparent biases are associated with the Indian monsoon in JJA season. The SWCF (Fig. 8) geographical pattern is also well simulated even in the subsidence regions west from the continents, which was rather encouraging.

Even though the SP-CAM tends to underestimate the low-level cloud fraction, the SP grid resolution may be sufficient to resolve anvil clouds created by deep convection as well as stratiform and cirrus clouds as the result of large-scale motions. One can see in Fig. 9 that the SP-CAM is indeed able to simulate the global distribution of clouds above 400-mb level rather well. In contrast, the standard CAM tends to significantly overestimate the high-cloud fraction.

The plots for the zonal-mean precipitation rate, precipitable water, OLR, absorbed solar radiation (ASR), LWCF, and SWCF are given by Fig. 10 for DJF and Fig. 11 for JJA. The simulated precipitation distribution is consistent with observations for both seasons. An obvious exception is the JJA precipitation bias associated with the Asian monsoon. It is interesting that apart from the Tropics, the zonal precipitation by the SP-CAM is basically identical to CAM precipitation in the extratropics and midlatitudes. Simulated precipitable water shows a rather good agreement with the National Aeronautics and Space Administration (NASA) Water Vapor Project (NVAP) dataset, with the SP-CAM showing a tendency to produce relatively more humid conditions around the equator. Both CAM and SP-CAM tend to exhibit the same moist bias of up to 5 mm in the extratropics between 30° and 50°S. The zonal-mean OLR and ASR and the ERBE data show a good

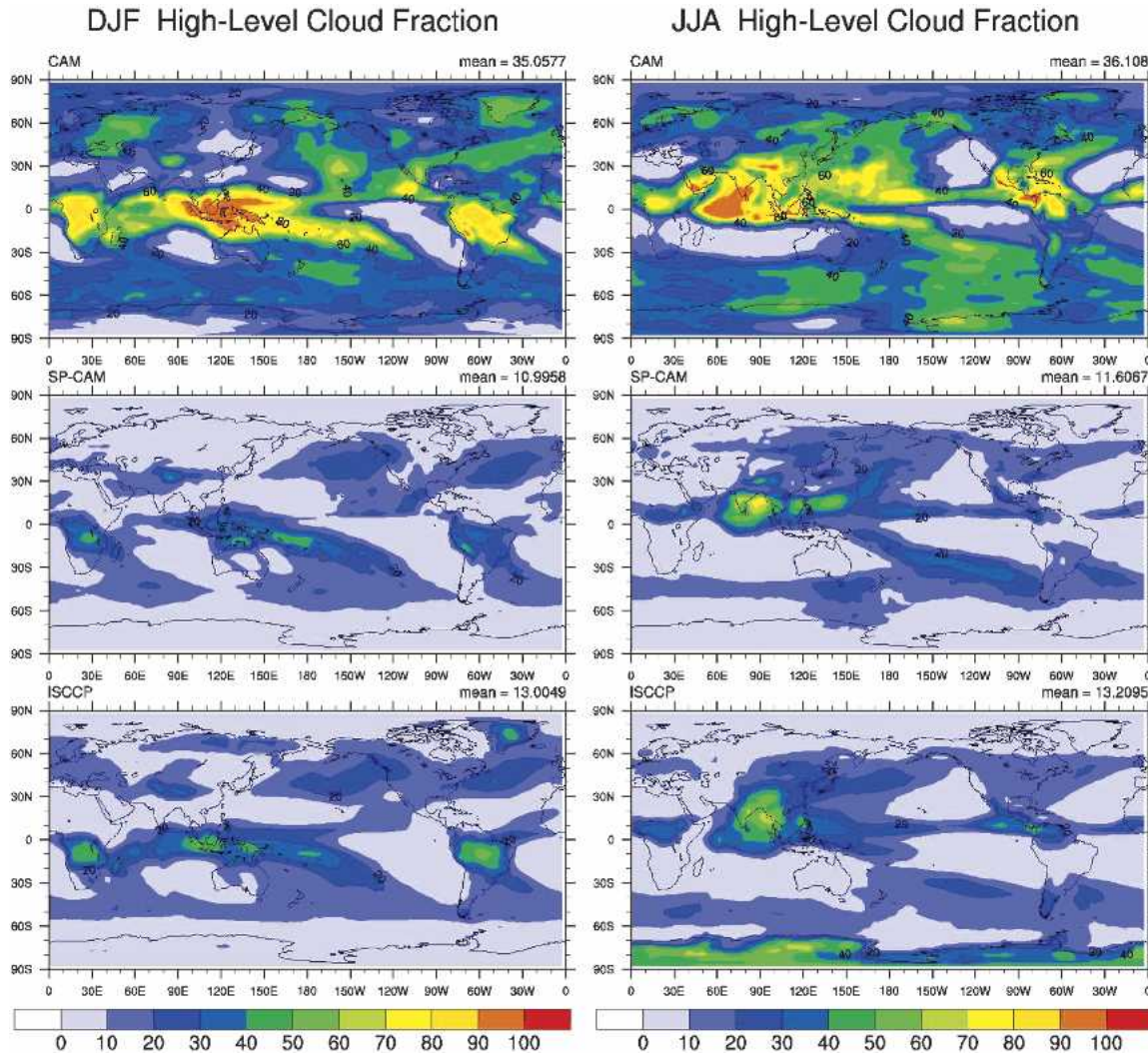


FIG. 9. As in Fig. 3, but for high-level cloud fraction (above 400-mb level).

agreement. For OLR, the largest biases exist in equatorial regions for DJF, and in the extratropics for JJA. The model also tends to overestimate the ASR in the extratropics due to a reduced amount of low-level clouds. The SP-CAM reproduces all three maxima of the zonal-mean LWCF rather well for both seasons; however, it significantly underestimates the LWCF in the Tropics. The SWCF compares well to ERBE for both seasons.

The biases in the zonal structure of the temperature field, as compared to the ECMWF reanalysis separately for DJF and JJA, are demonstrated by Fig. 12. One can see that the SP-CAM has a spatial pattern of biases that looks qualitatively very similar to that produced by CAM; however, the biases are quantitatively larger for the SP-CAM. Overall, the tropospheric biases are relatively small. The significant cold bias in the Tropics is associated with the tropopause being too high com-

pared to observations. A similar bias pattern of CAM and SP-CAM, despite different treatment of clouds, suggests that understanding the nature of those biases in the standard CAM may help reduce them in the SP-CAM as well.

#### *b. Frequency and diurnal variability of precipitation*

One of the important tests of any GCM is the ability to simulate the observed climatology of diurnal variations of precipitation over the ocean and land, in response to the diurnal solar heating. In this paper, we present some preliminary results of simulated timing of precipitation frequency maximum and the global distribution of the wet-day probability. The latter is defined as the percentage of days with nondrizzle precipitation over some time period, for example, a season. The ob-

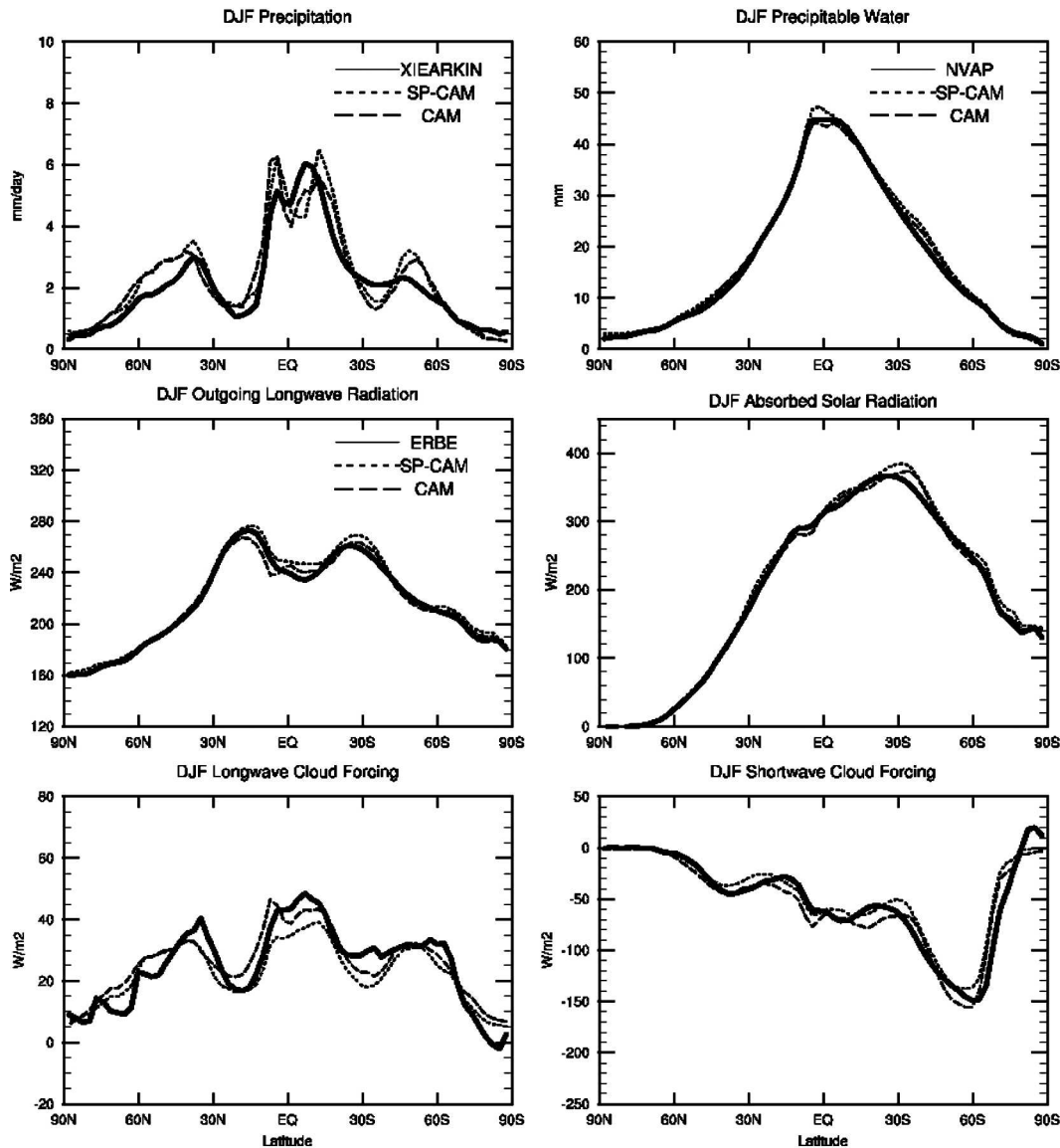


FIG. 10. DJF zonal mean of observed and simulated precipitation rate, precipitable water, outgoing longwave, and absorbed solar radiation, longwave cloud radiative forcing, and shortwave cloud radiative forcing. The simulations were performed with the standard CAM and the SP-CAM.

servational dataset created and described in detailed by Dai (2001) has been used for comparison. The season-mean diurnal cycle of the nondrizzle precipitation frequency was computed from the simulated 3-hourly precipitation rates. A 3-h-long sample was counted as containing a nondrizzle precipitation event if the mean precipitation rate over that time period was in excess of 1 mm day<sup>-1</sup>. The wet-day probability was computed by dividing the number of days that had at least one nondrizzle event by the total number of days in a season.

Figures 13 shows the global distribution of the local solar time of nondrizzle precipitation frequency maximum and wet-day probability for the Northern Hemisphere summer when the local cloud-surface interac-

tions become more important than synoptically driven weather in winter. It is generally well-known from ground and satellite observations (e.g., Imaoka and Spencer 2000; Lim and Suh 2000; Dai 2001) that in Tropics and summertime extratropics, the nondrizzle showery precipitation tends to occur most frequently in late afternoon, around 1400–1600 local solar time (LST) over the land, and in early morning, around 0500–0700 LST, over the oceans. One can see that the SP-CAM tends to reproduce this behavior quite well. The CAM, while being able to capture the correct timing in late morning-early afternoon over land, which is not consistent with the observations. Note that in the

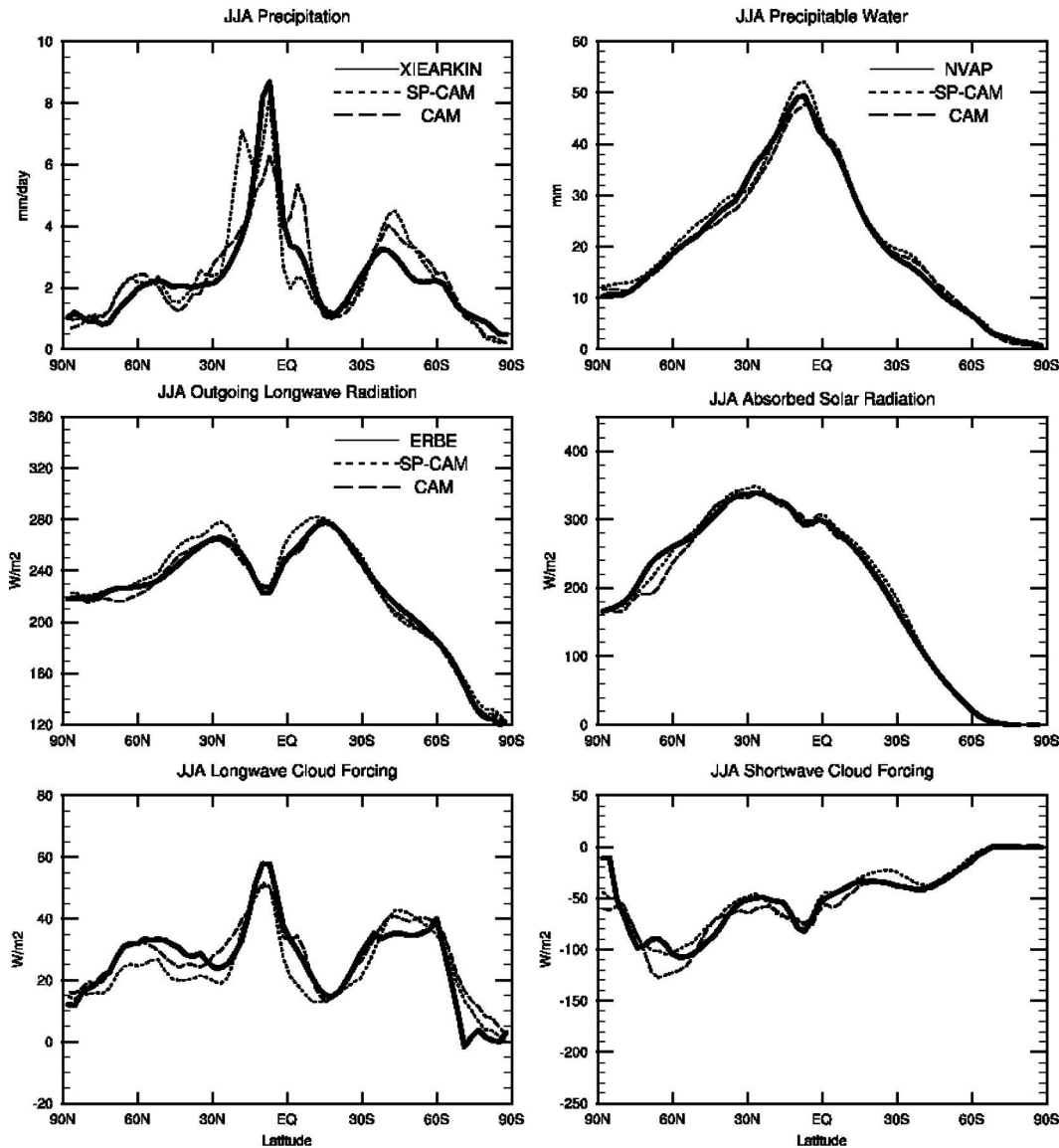


FIG. 11. As in Fig. 10, but for JJA.

Southern Hemisphere, the timing of the precipitation frequency maximum in the extratropics becomes quite uncertain because the precipitation is associated mostly with synoptic-scale weather systems rather than with local surface-atmosphere interactions.

### c. Tropical variability

In this section, we present the results of limited analysis of intraseasonal variability in the tropical regions, as this is historically an area where model performance is poor (e.g., Slingo et al. 1996). We present results that include all time scales, and similar analyses for 20–100-day bandpass-filtered data, since intraseasonal variability with 30–70-day periodicity is the dom-

inant mode of variability in the Tropics. The most common mode of variability is the MJO, which is a deep baroclinic, convectively coupled, eastward-propagating disturbance with the period of 40–80 days. It is most clearly visible in zonal wavenumbers 1–2 for the dynamical fields, and wavenumbers 1–3 for the OLR and precipitation fields. Most GCMs underestimate variability on these timescales when compared to simulated variability at higher frequencies and when compared to observations (Slingo et al. 1996).

Wavenumber–frequency spectra of 200-mb winds ( $U_{200}$ ) and OLR as observed and from the two model runs are shown in Fig. 14. We use the method of Wheeler and Kiladis (1999) in which the ratio of spectral signal to estimated background power is plotted. In

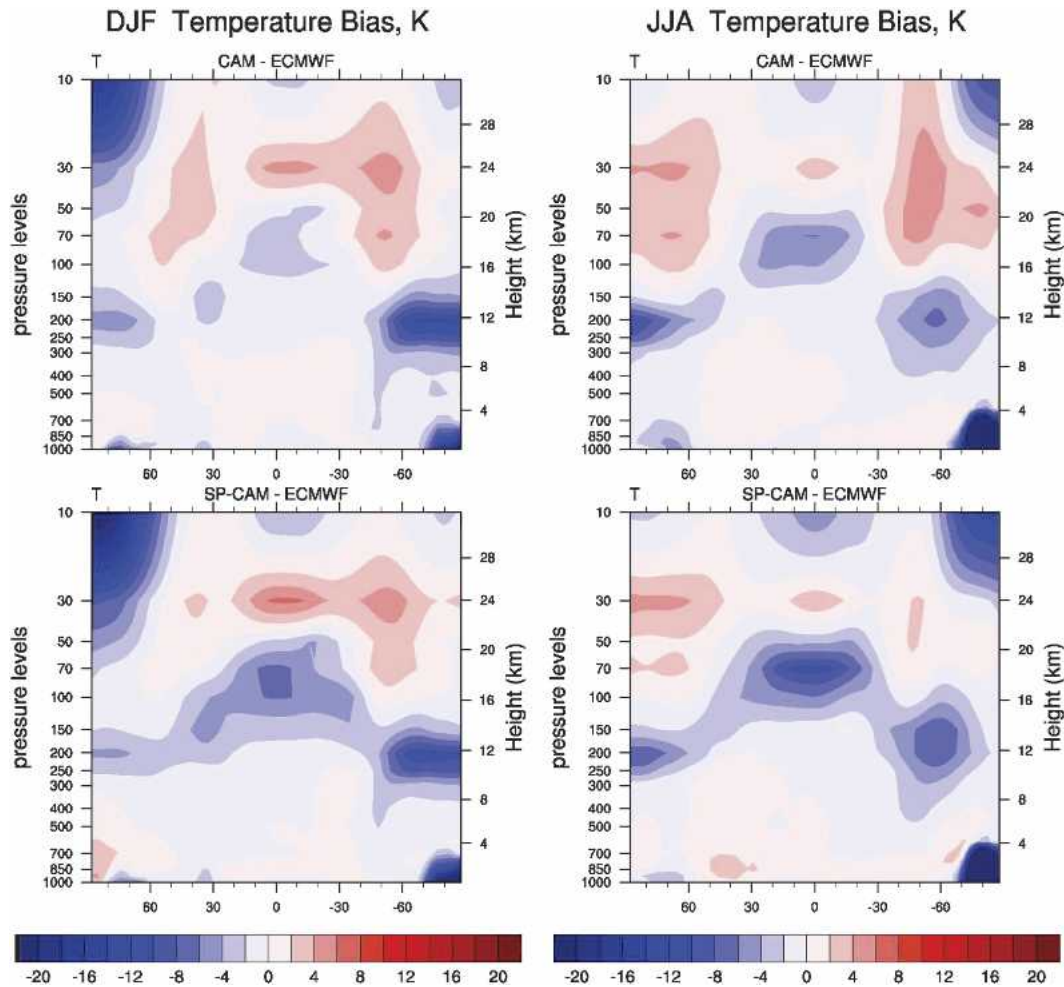


FIG. 12. (left) DJF and (right) JJA zonal mean bias of simulated temperature with respect to the European Centre for Medium-Range Weather Forecasts (ECMWF) reanalysis data for the simulations were performed with the standard CAM and the SP-CAM.

the U200 wind field, the National Centers for Environmental Prediction (NCEP) reanalysis reveals a high signal-to-noise ratio (SNR) at wavenumber 1 (positive wavenumbers indicate eastward propagation) for periods greater than about 30 days, illustrating the dominance of the MJO at tropical latitudes. High SNR is also found in fast-moving Kelvin waves on the right-hand side of the figure aligned with the Kelvin wave dispersion curves. In contrast, the CAM run has too high SNR at high-frequency, high-wavenumber disturbances. At MJO frequencies, the highest SNR is found in negative wavenumbers, or westward-moving disturbances. Replacing the traditional cumulus parameterization with the superparameterization slightly reduces the high SNR at higher frequencies, but more importantly, now puts the bulk of spectral power in the wavenumber–frequency space associated with the MJO.

The case for OLR is similar. Both the MJO and Kel-

vin waves are readily apparent in the NOAA OLR data. In the CAM run, however, low-frequency power shows no preferred wavenumber, and too much power is found in the high-frequency Kelvin waves. In the SP-CAM run, evidence of MJO activity is clear, although still not as clearly defined as it is in the observations. Still, it appears that the use of the superparameterization has improved the representation of the MJO over the control.

We next extract the portion of the variability that is defined by the wavenumber–frequency space associated with the MJO signal via an inverse Fourier transform. By computing the variability of this MJO signal, we can compare the geographic distribution of such variability in the models to its distribution in the real world. Because the MJO disturbance is predominantly a symmetric disturbance, only the symmetric part of the variability is plotted in Fig. 15. In the NCEP reanalysis (Fig. 15a), the largest variability in 200-mb winds is seen

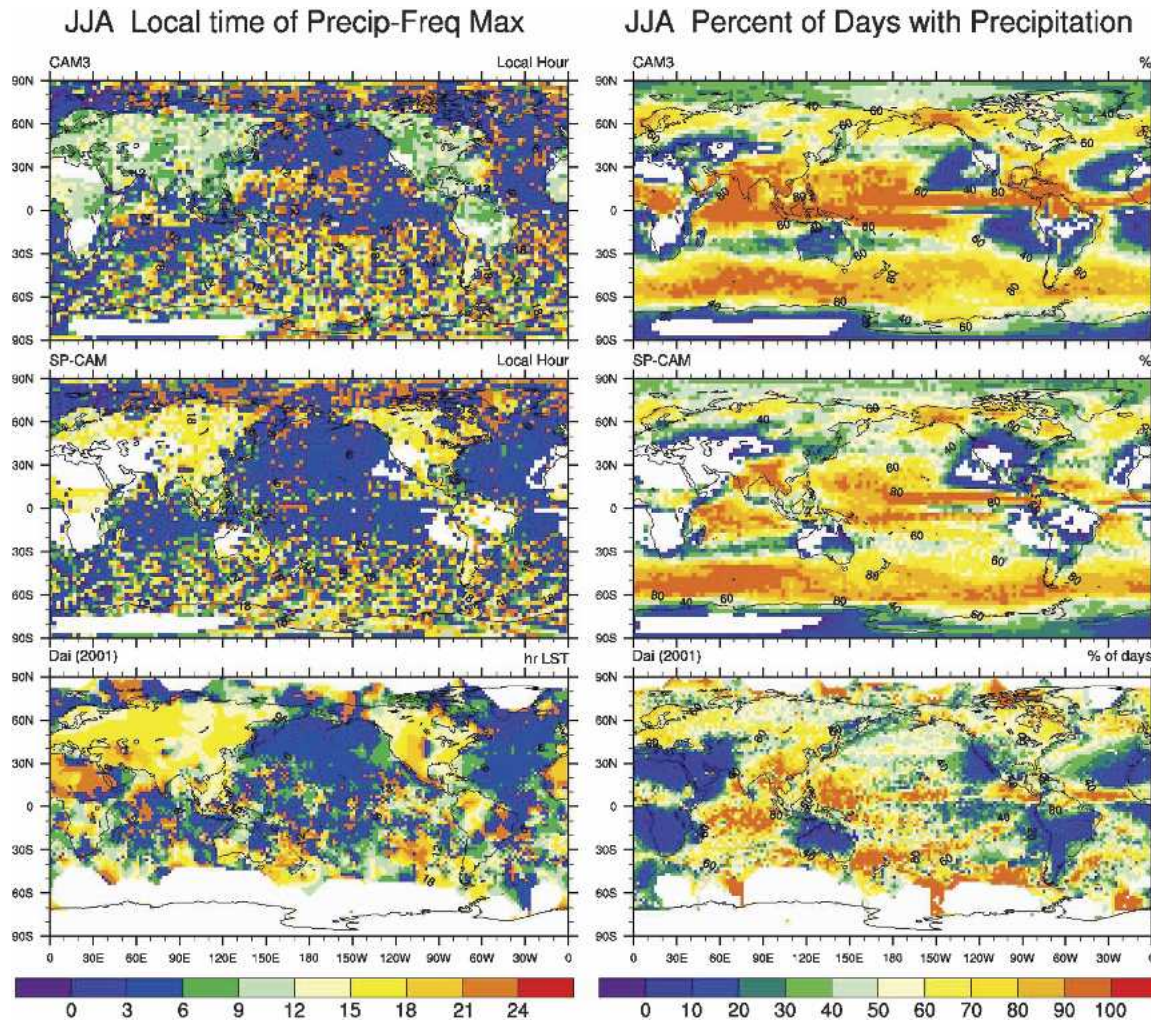


FIG. 13. JJA geographical distribution of (left) the local time of nondrizzle precipitation frequency maximum and (right) the percent of days with nondrizzle precipitation, as simulated with (upper) the standard CAM, (middle) SP-CAM, and (lower) from the dataset by Dai (2001).

over the eastern Pacific Ocean, with a secondary region of high MJO variability in the western Pacific, extending well into the sub-Tropics. The CAM run exhibits much weaker variability with minima at all subtropical longitudes. The SP-CAM run (Fig. 15c) is an improvement over the CAM run, with maxima in approximately the right locations, but with excessive variability. The improvement of the super parameterization over the standard model is better noted in the OLR fields (Figs. 15d–f). OLR variability in the CAM run is very weak, and there is little longitudinal variability. In contrast MJO OLR variability in the SP-CAM run is both of an appropriate magnitude and location.

#### d. Tropical biases and domain geometry

As discussed above, using the SP-CAM based on the 2D SP, lead to a significant problem: all the simulations

produced an unrealistically humid and rainy region in the tropical western Pacific, during the Northern Hemisphere summer (see Fig. 3). The nature of the bias in the western Pacific in JJA has not been understood by the time of submission of this paper. This problem seems to go away through the use of a 3D SP. The 3D SP has the same number of grid columns as the 2D SP, namely 64, but in the 3D SP these are arranged in an  $8 \times 8$  square rather than in a line. The grid spacing is 4 km in both horizontal dimensions, with doubly periodic boundary conditions, for a very limited CSR domain size of 32 km in each direction. Such a size is certainly too small to accommodate any mesoscale structure of a squall line, but is sufficient to accommodate individual deep updrafts. Having the same number of grid columns (64) as the 2D SP, the 3D SP is, nonetheless, more than 50% more expensive to run because of the extra terms in the prognostic equations associated with the

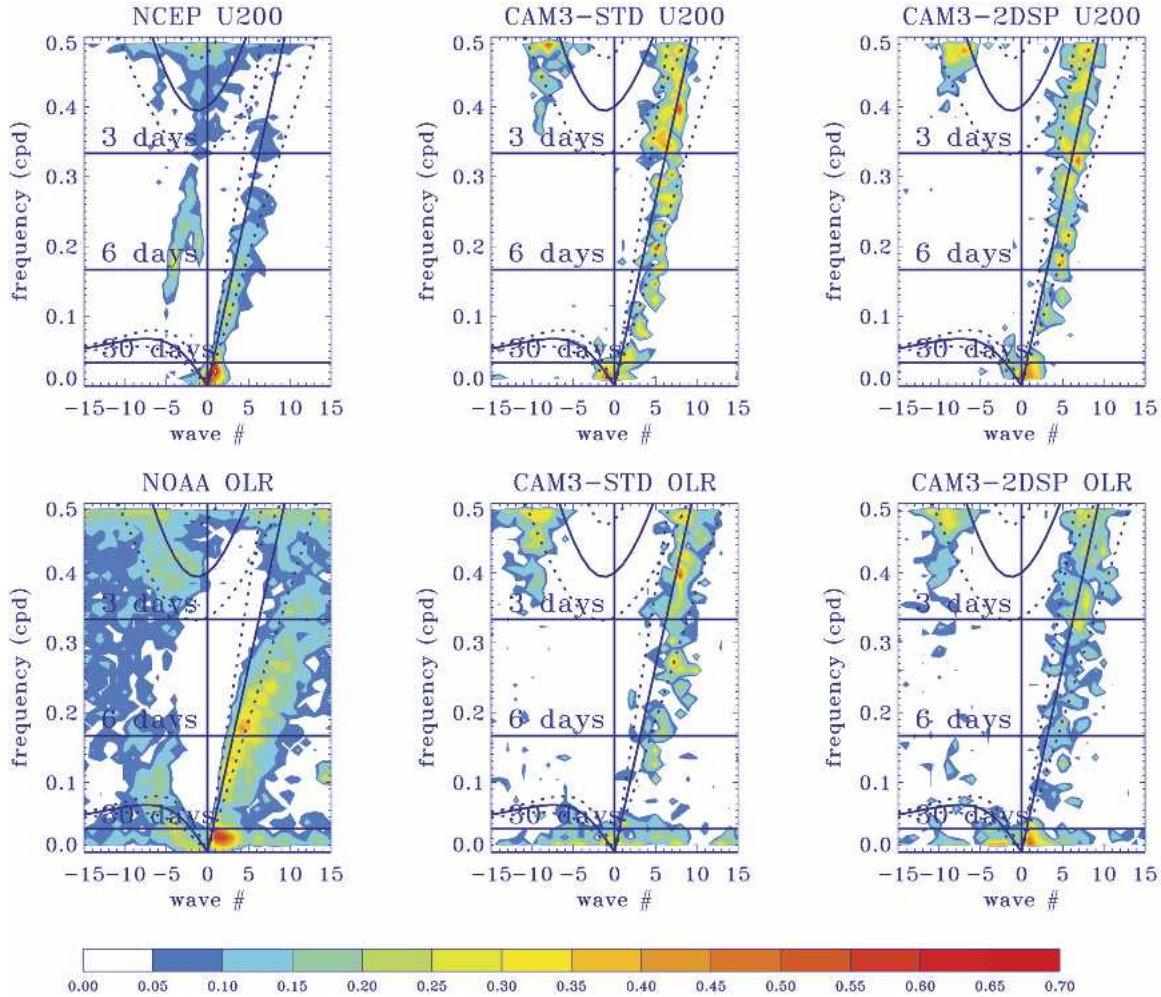


FIG. 14. Contour plots of  $\log_{10}$  (signal-to-noise ratio) for equatorially symmetric components of (upper) 200-hPa zonal winds and (lower) OLR. SNR is computed as in Wheeler and Kiladis (1999), where the background spectra are estimated by successively smoothing the raw 2D power spectra. Dispersion relations for equivalent depths of 125 (dashed), 250 (solid), and 500 m (dotted) are shown for Kelvin, mixed Rossby-gravity, and internal gravity waves. CAM3-STD and CAM3-2DSP refer to the standard CAM and SP-CAM, respectively.

additional dimension. Currently, a larger 3D-SP domain would be computationally prohibitive.

Two runs with the 3D SP have been carried out. One run was similar to the 2D SP runs in that the large-scale momentum transport due to the SP convection was not allowed to feed back to the GCM. In the second run, we have included the effects of cloud-scale momentum transport on the large-scale circulation. The JJA distribution of precipitation for these two runs is shown in Fig. 16. One can see that in both 3D SP runs, the precipitation bias in the western Pacific has been mitigated. It is interesting that the double ITCZ problem is quite pronounced in the 3D SP run without momentum coupling, but seems to go away in the run with the included momentum transport. This suggests that adequate parameterization of the momentum transport by convection may be required in order to alleviate the double-ITCZ problem in climate models (e.g., Wu et al. 2003).

#### 4. Summary

Since Khairoutdinov and Randall (2001) reported their first results of modeling the earth's atmospheric general circulation using a CRM as the superparameterization of clouds in a realistic GCM, NCAR CAM, about a dozen T42-resolution runs, each up to 500 days long, have been performed. In our research involving the superparameterized version of CAM, SP-CAM, we have been rather severely constrained by the available computational resources needed to run the model more than 200 times more expensive than the standard CAM, although we have demonstrated that SP-CAM can be efficiently run on more than a thousand processors. For a traditional GCM model development, a dozen yearly runs is hardly sufficient amount of experience to gain confidence in the models performance and to address its deficiencies. Definitely, the SP-CAM is still in a

## MJO-filtered fields, symmetric part

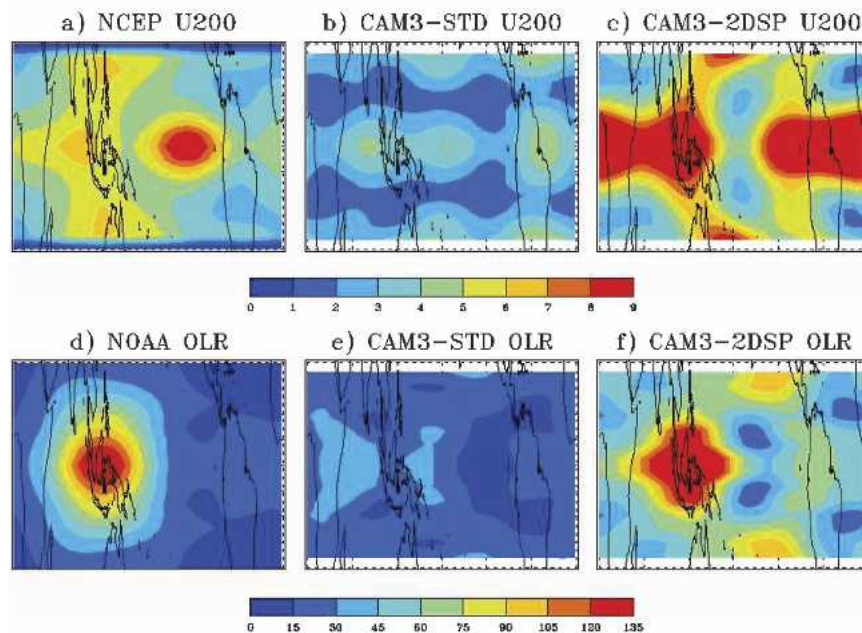


FIG. 15. Geographic distribution of symmetric MJO variance of (a)–(c) 200-hPa zonal winds and (d)–(f) OLR. The MJO signal is computed via an inverse Fourier transform of the coefficients corresponding to eastward-moving waves with zonal wavenumbers 1–4 and periodicities in the 20–70-day range. To simplify the display, the transform is applied to the equatorially symmetric time series, which accounts for nearly 80% of the total variance near the equator.

rather active development phase; nevertheless, we decided to document our early experiences with the SP-CAM, which we feel could be of interest to the atmospheric science community, especially considering the unique nature of such a GCM.

The results from the most recent 500-day long simulation of the atmospheric general circulation using a 2D SP based on a 2D CRM with 64 grid columns were contrasted with those of a control run performed using the conventional cloud parameterizations. In terms of the mean state, the SP-CAM produces quite reasonable geographical distributions of precipitation, precipitable water, top-of-atmosphere radiative fluxes, cloud radiative forcing, and high-cloud fraction for both seasons. The most notable and persistent bias apparent in all the SP simulations was associated with anomalously strong precipitation in the Western Pacific for the summer months.

It is apparent that the SP-CAM exhibits much improved diurnal variability of nondrizzle precipitation frequency in terms of the diurnal cycle. Over the summertime land masses, the control model tends to precipitate most frequently around local solar noon, which is a few hours earlier than observations suggest. In contrast, the SP model tends to peak precipitation frequency during late afternoon hours, in accord with observations. Over the ocean, both models precipitate

most frequently in the early morning hours as observed. The SP model global distribution of the percentage of days with nondrizzle precipitation compares to observed distribution most favorably, while the standard model tends to precipitate by about 20%–30% more frequently. The global distribution of the wet-day probability as simulated by the SP-CAM agrees rather well with observations in both the spatial patterns and amplitudes. The standard CAM, although generally agreeing with observations in spatial patterns, tends to overestimate the observed frequency of precipitation, especially in the Tropics. The SP model seems to improve the convective intraseasonal variability over the standard model. Our preliminary results suggest that the SP produces much more realistic variability of such fields as 200-mb wind and OLR than the control, including the MJO.

All the simulations based on the 2D SP have featured an unrealistically rainy region in the tropical western Pacific, during the Northern Hemisphere summer. The problem seems to be mitigated when the 2D SP is replaced with a 3D SP that uses the same number of grid columns and horizontal resolution as the 2D SP, but arranges them in an  $8 \times 8$  pattern. In one of two runs with the 3D SP, the large-scale momentum transport due to the SP convection was allowed in contrast to the 2D SP-CAM. Interestingly, the double ITCZ

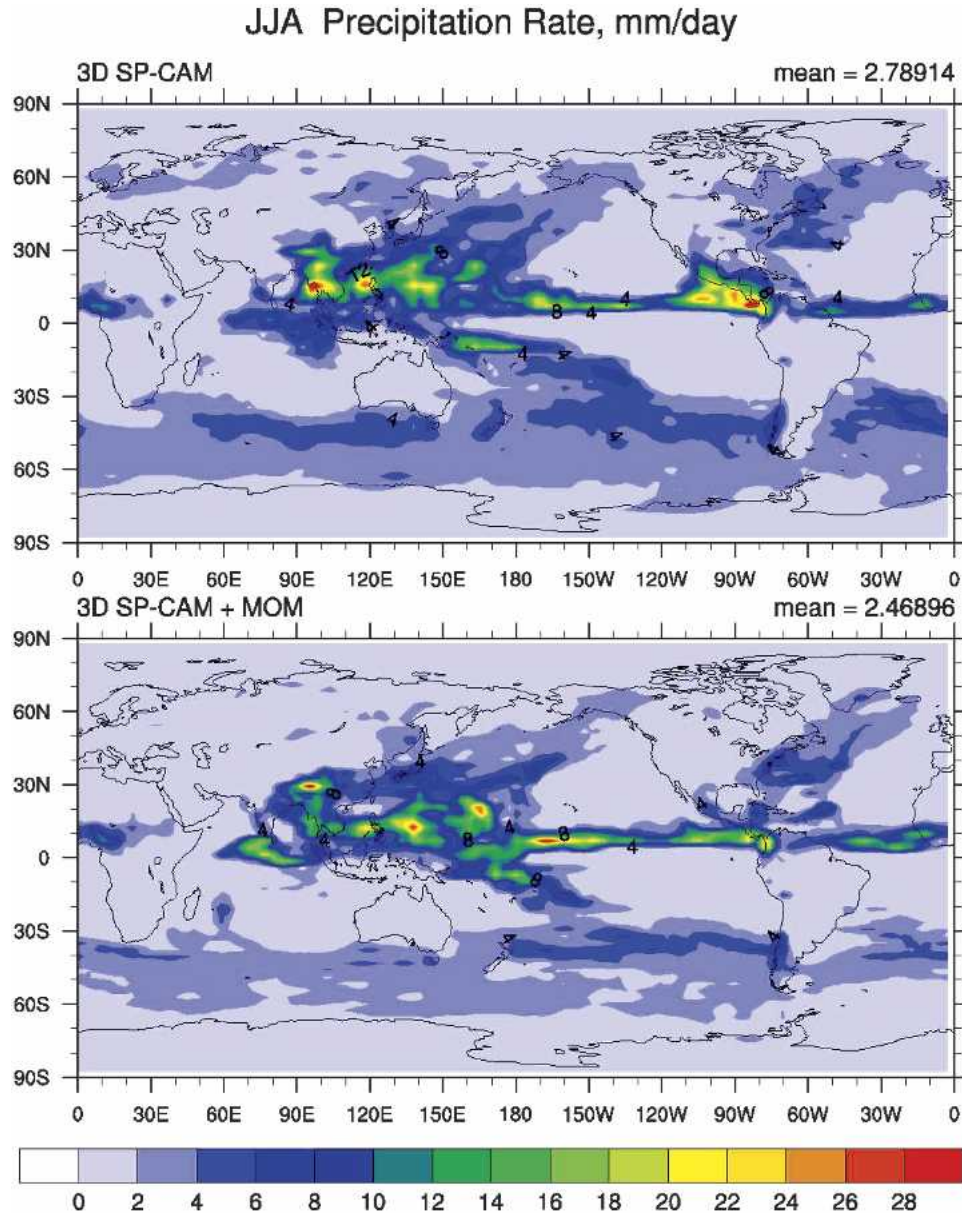


FIG. 16. Mean JJA total precipitation as simulated with the SP-CAM with the 3D SP using  $8 \times 8 \times 24$  gridpoint domain (upper) without and (lower) with large-scale momentum transport by convection.

problem, which is quite pronounced in all the 2D SP runs and in the 3D SP run without momentum coupling, seems to go away in the run with the momentum transport.

One can argue that a small-domain 3D CRM may still represent a much better physical framework than the entraining-plume models typically used in convective parameterizations, since a set of physical equations is solved, and many closure assumptions are avoided. However, we have been reluctant to immediately replace the 2D SP by the small-domain 3D SP for the

future SP-CAM runs until the effects of eliminating the mesoscales are studied and better understood. In conclusion, we note that the smallness of the domain itself does not seem to be responsible for the apparent improvement in the JJA precipitation pattern. A similar experiment done using a small-domain 2D SP with only 8-grid column showed the biases that were very similar to those found in the 64-column 2D-SP runs. Further research into effects of the SP domain dimensionality and size on simulated atmosphere general circulation is therefore warranted.

*Acknowledgments.* We thank Auguo Dai for providing a dataset on observed precipitation frequencies. The computations were performed using the IBM SP supercomputers “Blackforest” at the National Center for Atmospheric Research and “Seaborg” at the National Energy Research Scientific Computing Center. Support for this research has been provided by the U. S. Department of Energy through Grant DE-FG03-95ER61968 and National Science Foundation Grant ATM-9812384, both to Colorado State University.

## REFERENCES

- Arakawa, A., 2004: The cumulus parameterization problem: Past, present, and future. *J. Climate*, **17**, 2493–2525.
- Betts, A. K., and M. J. Miller, 1986: A new convective adjustment scheme. Part II: Single column tests using GATE wave, ATEX and Arctic Air mass data sets. *Quart. J. Roy. Meteor. Soc.*, **112**, 693–709.
- Blackmon, M., and Coauthors, 2001: The Community Climate System Model. *Bull. Amer. Meteor. Soc.*, **82**, 2357–2376.
- Cole, J. N. S., H. W. Barker, D. A. Randall, M. F. Khairoutdinov, and E. E. Clothiaux, 2005: Global consequences of interactions between clouds and radiation at scales unresolved by global climate models. *Geophys. Res. Lett.*, **32**, L06703, doi:10.1029/2004GL020945.
- Dai, A., 2001: Global precipitation and thunderstorm frequencies. Part II: Diurnal variations. *J. Climate*, **14**, 1112–1128.
- Grabowski, W., 2001: Coupling cloud processes with the large-scale dynamics using the cloud-resolving convection parameterization (CRCP). *J. Atmos. Sci.*, **58**, 978–997.
- , X. Wu, M. W. Moncrieff, and W. D. Hall, 1998: Cloud-resolving modeling of cloud systems during Phase III of GATE. Part II: Effects of resolution and the third spatial dimension. *J. Atmos. Sci.*, **55**, 3264–3282.
- Imaoka, K., and R. W. Spencer, 2000: Diurnal variation of precipitation over the tropical oceans observed by TRMM/TMI combined with SSM/I. *J. Climate*, **13**, 4149–4158.
- Khairoutdinov, M. F., and D. A. Randall, 2001: A cloud resolving model as a cloud parameterization in the NCAR Community Climate System Model: Preliminary results. *Geophys. Res. Lett.*, **28**, 3617–3620.
- , and —, 2003: Cloud resolving modeling of the ARM Summer 1997 IOP: Model formulation, results, uncertainties, and sensitivities. *J. Atmos. Sci.*, **60**, 607–625.
- Lim, G.-H., and A.-S. Suh, 2000: Diurnal and semidiurnal variations in the time series of 3-hourly assimilated precipitation by NASA GEOS-1. *J. Climate*, **13**, 2923–2940.
- Madden, R. A., and P. R. Julian, 1994: Observations of the 40–50-day tropical oscillation—A review. *Mon. Wea. Rev.*, **122**, 814–837.
- Randall, D. A., M. F. Khairoutdinov, A. Arakawa, and W. W. Grabowski, 2003a: Breaking the cloud-parameterization deadlock. *Bull. Amer. Meteor. Soc.*, **84**, 1547–1564.
- , and Coauthors, 2003b: Confronting models with data: The GEWEX Cloud Systems Study. *Bull. Amer. Meteor. Soc.*, **84**, 455–469.
- Slingo, J. M., and Coauthors, 1996: Intraseasonal oscillations in 15 atmospheric general circulation models: Results from an AMIP diagnostic subproject. *Climate Dyn.*, **12**, 325–357.
- Wheeler, M., and G. N. Kiladis, 1999: Convectively coupled equatorial waves: Analysis of clouds and temperature in the wavenumber–frequency domain. *J. Atmos. Sci.*, **56**, 374–399.
- Williamson, D. L., and J. G. Olson, 1994: Climate simulations with a semi-Lagrangian version of the NCAR community climate model. *Mon. Wea. Rev.*, **122**, 1594–1610.
- Wu, X., X.-Z. Liang, and G. J. Zhang, 2003: Seasonal migration of ITCZ precipitation across the Equator: Why can’t GCMs simulate it? *Geophys. Res. Lett.*, **30**, 1824–1827.
- Xie, P., and P. A. Arkin, 1996: Analyses of global monthly precipitation using gauge observations, satellite estimates, and numerical model predictions. *J. Climate*, **9**, 840–858.
- Xu, K.-M., and D. A. Randall, 1996: Explicit simulation of cumulus ensembles with the GATE Phase III data: Comparison with observations. *J. Atmos. Sci.*, **53**, 3710–3736.
- , and Coauthors, 2002: An intercomparison of cloud-resolving models with the Atmospheric Radiation Measurement summer 1997 Intensive Observation Period data. *Quart. J. Roy. Meteor. Soc.*, **128**, 593–624.